

3D Printing of $\text{Na}_{1.3}\text{Al}_{0.3}\text{Ti}_{1.7}(\text{PO}_4)_3$ Solid Electrolyte via Fused Filament Fabrication for All-Solid-State Sodium-Ion Batteries

Aycan C. Kutlu,^{*[a]} Dorit Nötzel,^[b] Carlos Ziebert,^[a] Hans J. Seifert,^[a] and Ijaz Ul Mohsin^[a]

All solid-state batteries pave the way to safer batteries as they do not contain flammable components and allow potentially higher energy densities through the direct use of alkali metals as anode materials. However, the applicability of solid electrolytes is hindered by their slower diffusion kinetics and charge transfer processes compared to liquid electrolytes. The purpose of this study is to investigate the electrochemical performance of 3D printed ceramic electrolyte. Prepared filaments were printed with optimized parameters and the polymeric binders were subsequently removed by solvent-/thermal debinding followed by a sintering process. The most reliable prints were

performed with 58 vol% filled feedstock and the highest densities of sintered specimen were measured at a sintering temperature of 1100 °C with $(94.27 \pm 0.37)\%$ and $(94.27 \pm 0.07)\%$ for printed and pressed samples, respectively. The lowest impedances for 3D printed samples were measured for 1100 °C sintered specimen, yielding conductivities of $(1.711 \pm 0.166) \times 10^{-4} \text{ S cm}^{-1}$ at 200 °C. Stripping/plating tests performed at 60 °C confirmed the feasibility of 3D printed electrolytes realized by Fused Filament Fabrication (FFF) for the application in solid-state batteries.

Introduction

With the advancing electrification in the automotive sector and stationary energy storage for regenerative energy sources, the demand for lithium has increased immensely and hence its price.^[1] Sodium is an excellent alternative due to its substantial abundance and chemical similarity.^[2] Furthermore, a cost reduction of 30% is estimated for the sodium-ion technology compared to the lithium-ion battery technology.^[3]

Conventional batteries use a liquid organic electrolyte that poses a safety risk due to its flammability. One approach to mitigate this safety issue is the use of all-solid-state batteries (ASSB), wherein the liquid electrolyte is replaced by a solid electrolyte (SE).^[4] As recent reports show, solid electrolytes are believed to suppress dendrite growth owing to their lower electronic conductivities and mechanical properties.^[5] However,

this is still a topic of debate which needs to be addressed. Typically, solid-state electrolytes are broadly classified into two types depending on their chemical structure, namely, organic (polymer) and inorganic (ceramic oxides and sulphides) compounds.^[6] Oxide based solid electrolytes have the advantage of air stability, thermal stability and cathodic stability even at higher voltages of > 4.5 V, which is advantageous for high energy density applications.^[7] Considering NASICON ($\text{Na}_x\text{MM}'(\text{PO}_4)_3$ with M and M' being metals) based systems, they demonstrate high ionic conductivities of up to $1 \times 10^{-3} \text{ S cm}^{-1}$ at room temperature.^[6]

The conventional way of producing oxide based solid electrolytes follows the typical powder technological process routine. The material in powder form is placed in a mold where it gets compressed in a uniaxial or isostatic press to produce a green part, which is then sintered to achieve densification of the pellet.^[8] Due to the geometric limitation in pressing processes, only simple geometries such as disk-shaped or sandwich structures can be fabricated. This restrains the possibilities for optimization by realizing sophisticated cell architectures to achieve larger interfacial areas. By implementing 3D-structured electrolytes and electrodes, the interface of the active material vs the electrolyte can be increased. By optimizing the design of the electrodes/electrolyte architecture, the diffusion path length of the ions can be shortened, which results in improved rate performance of the battery.^[9] 3D printing is one way of implementing this structuring of batteries, as any design can be printed and no fixed geometries are imposed by pressing molds. The layer-by-layer principle in 3D printing enables the production of desired thick electrode layers.^[10] There are many different types of 3D printing techniques with their specific advantages and disadvantages.^[11] Batteries and their components are often printed using the

[a] A. C. Kutlu, Dr. C. Ziebert, Prof. Dr. H. J. Seifert, Dr. I. Ul Mohsin
Institute of Applied Materials – Applied Materials Physics (IAM-AWP),
Karlsruhe Institute of Technology, Karlsruhe, Germany
E-mail: Aycan.Kutlu@kit.edu
Homepage: http://www.iam.kit.edu/awp/21_1288.php

[b] Dr. D. Nötzel
Institute of Applied Materials – Materials Science and Engineering (IAM-WK), Karlsruhe Institute of Technology, Karlsruhe, Germany

Supporting information for this article is available on the WWW under <https://doi.org/10.1002/batt.202300357>

This publication is part of a joint Special Collection dedicated to Post-Lithium Storage, featuring contributions published in Advanced Energy Materials, Batteries & Supercaps, and ChemSusChem.

© 2023 The Authors. *Batteries & Supercaps* published by Wiley-VCH GmbH. This is an open access article under the terms of the Creative Commons Attribution Non-Commercial License, which permits use, distribution and reproduction in any medium, provided the original work is properly cited and is not used for commercial purposes.

direct ink writing (DIW) technique, in which a colloidal ink containing the battery material is formulated, and then deposited on a substrate, achieving fine details in the low tenths of a micron.^[12] McOwen et al.^[13] printed a solid lithium-ion conductor $\text{Li}_7\text{La}_3\text{Zr}_2\text{O}_{12}$ using well-tuned inks, and was able to fabricate various structures like “log-cabin” or stacked arrays, that could achieve a stable stripping/plating profile with current densities of 0.33 mA cm^{-2} at room temperature with a polarization below 10 mV. Liu et al. successfully 3D printed and sintered various two-dimensional shapes of $\text{Li}_{1.3}\text{Al}_{0.3}\text{Ti}_{1.7}(\text{PO}_4)_3$ using DIW, achieving an ionic conductivity of $4.24 \times 10^{-4} \text{ Scm}^{-1}$ for 3 layers, which decreased with subsequent layers down to $1.38 \times 10^{-4} \text{ Scm}^{-1}$ at 6 layers.^[14] However, the ionic conductivities achieved by the DIW printed ionic conductors do not yet reach the ionic conductivity that the material can achieve by conventional means.^[15] A second drawback is that additional process steps are necessary, such as extensive ball milling, before the ink is used or a post-treatment such as drying or freeze-drying, depending on the ink system used.^[13,14,16]

Another technique used for 3D printing of a battery or battery components is the Fused Filament Fabrication (FFF) method, in which the battery material is dispersed in a polymer binder system, forming a so-called feedstock, and the 3D printer is fed with the material in the form of a filament.^[17] This technique was used within this work. The advantages of this technology are the storability of the filaments, the safer handling of nanopowders as they are bound in the binder system, no organic solvent is used and that it offers an economically feasible solution. One disadvantage of producing full-ceramic printed parts is the time-consuming debinding of the specimens, during which the binder system is removed. Another disadvantage of the FFF technique is its low manufacturing precision as typical available nozzle sizes are between (0.15–0.8) mm leading to a lateral resolution in this order of magnitude, whereas typical achievable layer heights are between (50–200) μm . The shrinkage during the sintering step makes the structures even finer. Nevertheless, an interesting aspect of FFF 3D printing is that many samples can be produced quickly and in an automated manner in rapid succession, making sample production significantly less time-consuming compared to individual powder pressing. Batteries manufactured using FFF have so far shown significantly lower capacities than conventionally manufactured batteries, which is due to the large amount of binder material present in the batteries.^[17,18] However, Valera-Jiménez et al.^[19] demonstrated that high capacities of 168 mAh g^{-1} (C/2) and 129 mAh g^{-1} (10/C) could be achieved by debinding and sintering 3D printed $\text{Li}_4\text{Ti}_5\text{O}_{12}$ (LTO) and LiCoO_2 (LCO), respectively. Sotomayor et al.^[20] obtained full ceramic thick (470 μm) LTO electrodes using Powder Extrusion Molding (PEM), a technique also based on the use of a feedstock. They showed a more than two times higher capacity of 319 mAh cm^{-3} (C/24) compared to conventionally coated electrodes with 131 mAh cm^{-3} due to the dense and additive free design, as well as an improved electronic conductivity as a result of a thin carbon coating around the LTO particles, which formed due to the thermal treatment. A carbon coating of the ceramic particles that favors better electronic

conductivity was further confirmed by Transmission Electron Microscopy (TEM). Thus, such a coating represents an interesting design strategy for electrode materials. For the use of a SE, however, this would be fatal. Multi-materials printing can also be done by using the FFF method, which enables the printing of several components of the battery (e.g. anode, cathode, electrolyte) together, and several different commercial options for this technology exist.^[21] This results in the possibility of producing a complete battery in a single print with a wide variety of structures as shown schematically for a few examples in Figure S1.^[22,21]

In the present work, a commercially available sodium based $\text{Na}_{1.3}\text{Al}_{0.3}\text{Ti}_{1.7}(\text{PO}_4)_3$ (NATP, NEI Corp.) solid electrolyte with NaSiCON structure was chosen for the FFF printing owing to its commercial availability and air stability. The NATP powder was used with a PVB-based binder to prepare printable filaments that are used to produce printed solid electrolytes. Fused Filament Fabrication method was applied for the printing process and a careful analysis on the feedstock viscosity, sintered density, microstructure and conductivity was performed. Finally, the stripping/plating behavior of samples with an optimized density and microstructure was investigated. As a reference, pressed powder compacts of the same material were examined in the same way and compared with the 3D printed samples.

To the best of the authors' knowledge, fabrication of sodium based full ceramic electrolytes via FFF has not been published yet and therefore this work acts as a proof-of-concept study. Figure 1 shows the general fabrication process chain beginning with the feedstock preparation, where the electrolyte powder and organic binder components are mixed in an internal mixer that records the torque during the mixing process. The resulting feedstock is then extruded into filaments and used for 3D printing. The printed parts are first debinded in demineralized water and then thermally to remove all organic components, after which they are sintered in normal atmosphere. The sintered specimens are further characterized with Scanning Electron Microscopy (SEM), Nanoindentation, X-Ray Diffraction (XRD), Electrochemical Impedance Spectroscopy (EIS), Chronoamperometry (CA) and Chronopotentiometry (CP). The feedstock composition has been optimized to allow the highest possible loading of solid electrolyte at which 3D printing still works reliable. After the described two-step debinding, different sintering temperatures and their influence on density and microstructure formation have been investigated.

Results and Discussion

Disk-shaped samples were 3D printed, debinded and sintered to investigate the feasibility of fabricating solid electrolytes for the application in all-solid-state-sodium-ion batteries (ASSSB) using the FFF 3D printing process. The samples were compared with conventional sintered powder compacts to observe influences of the shaping process.

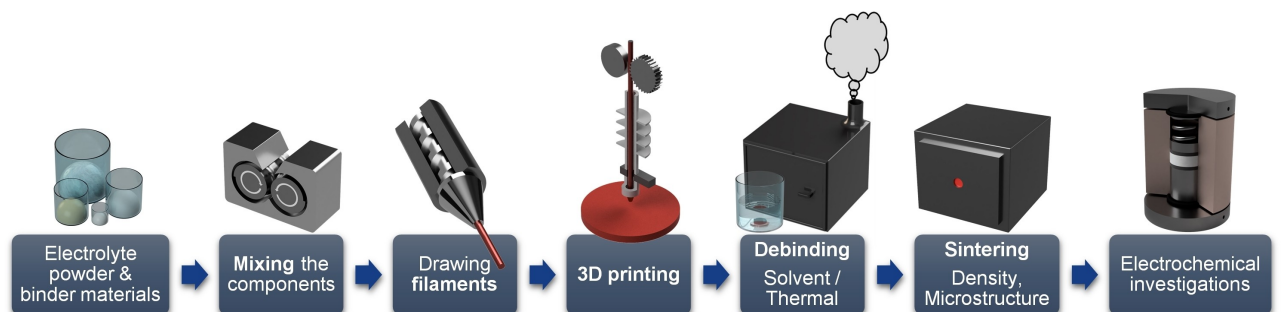


Figure 1. Schematic process chain for the fabrication of samples via the FFF method.

Feedstock characterization and 3D printing

Feedstocks with (55, 58 and 60) vol% of solid electrolyte powder were prepared using an internal mixer at 125 °C with continuous torque recording. The binder system consists of polyvinyl butyral (PVB), which provided sufficient green strength as a backbone, while polyethylene glycol (PEG) was used to reduce the viscosity of the feedstock. Lauric acid (LA) was added as a dispersing agent to homogeneously distribute the powder material in the binder system. The mixing process can be monitored and information about the state of mixing can be obtained from the progression of the torque over time.

The homogeneity of the powder distribution in the binder system is indicated by a constant torque. The recorded compounding torque is shown in Figure 2(a) and can roughly be separated into three regions. The filling zone at the beginning marks the introduction of the various feedstock components and shows a strong increase in torque, up to approx. 27 Nm, due to increased particle-particle interactions of the powder material. As the wetting of powder and binder material increases, the torque decreases (kneading zone) and reaches an equilibrium region at which a homogeneous distribution of the powder in the binder can be assumed (equilibrium zone).^[23] Measured final torque values for (55, 58

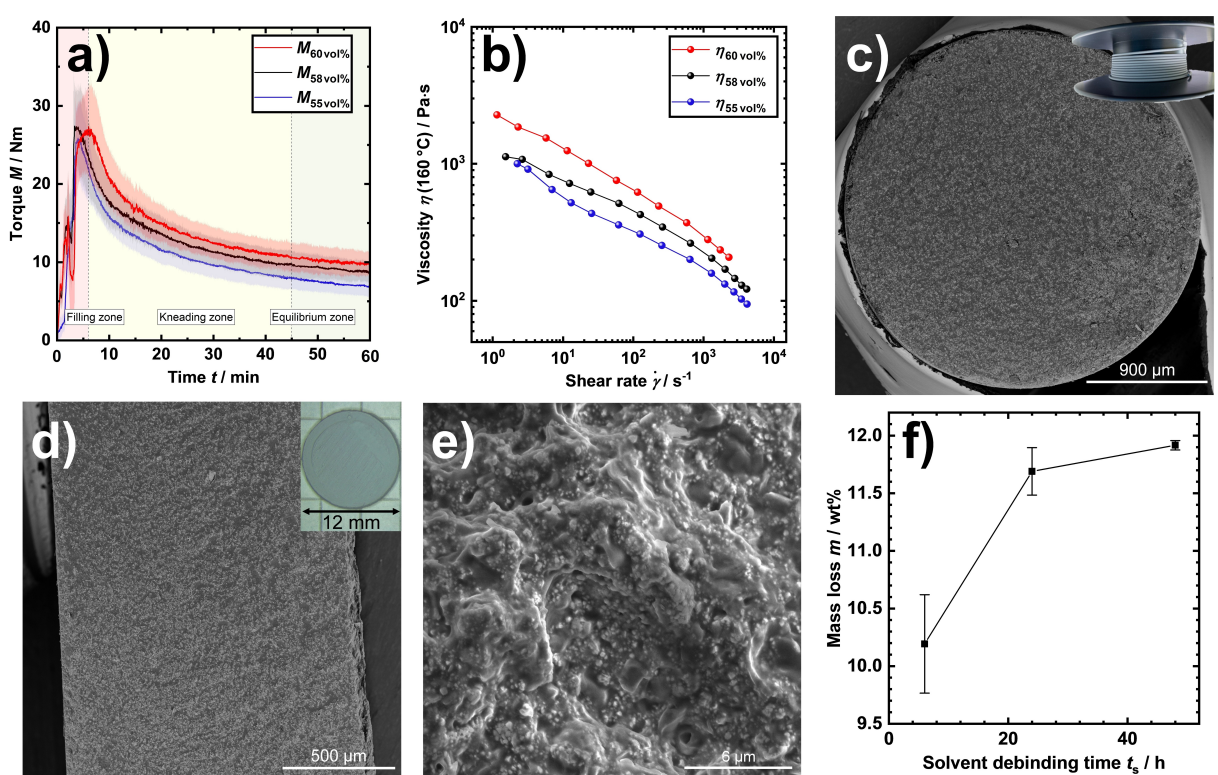


Figure 2. Characterization of feedstocks with 55, 58 and 60 vol % powder loading in a) torque time recording of compounding, b) viscosity vs. shear rate, c) extruded filament fracture surface (58 vol%) and wended filament spool as inset, d) 3D printed specimen fracture surface of liquid nitrogen cooled 3D printed green part (58 vol%), e) higher magnification of 3D printed specimen fracture surface, f) solvent debinding of 58 vol% filled feedstock at room temperature over debinding time.

and 60) vol% feedstocks are (6.9, 8.6 and 9.6) Nm, respectively. By increasing the powder concentration, increased particle-particle interactions are expected due to less binder in the system which results in an increase in the measured torque.

In order to make a preliminary assessment of the 3D printability, capillary rheological measurements were performed with the prepared feedstocks as shown in Figure 2(b) at the potential printing temperature of 160 °C. All feedstocks show a decreased viscosity with increasing shear rate, indicating shear thinning behavior. Viscosity values at a shear rate of 100 s⁻¹ were approx. 320 Pa·s for 55 vol%, 450 Pa·s for 58 vol% and 650 Pa·s for 60 vol% feedstock. An increase in powder concentration leads to an increased viscosity at all shear rates.^[24] The dispersed particles hinder the movement of the polymer chains and restrict the flow. In addition, as mentioned before, the probability of particle-particle interactions, and therefore the friction increases with increasing powder concentration.^[25] According to a rule of thumb, feedstocks with $\eta = 1000$ Pa·s at a shear rate of ~ 100 s⁻¹ are most likely printable, which is fulfilled for the feedstocks investigated.^[26]

Stearic acid is often used as a dispersant for feedstocks in ceramic injection molding and 3D printing.^[27] Typically, the filaments produced are too brittle to be wound up and printed from spools. The inset in Figure 2(c) shows that replacing stearic acid ($C_{18}H_{36}O_2$) with lauric acid ($C_{12}H_{24}O_2$) provides sufficient flexibility of the filaments to wind them onto commercial spools. Work by Heldele^[28] showed that lauric acid allows higher loadings of the ceramic in feedstocks and explained this by the shorter chain length of lauric acid compared to stearic acid, which leads to less interactions between dispersant and binder. Due to the lower interaction, rearrangement of dispersed particles is facilitated and results in increased flexibility.

Figure 2(c) shows a cryo-fractured cross-section of the filament. To prevent process errors such as over- or under-extrusion, the cylindrical shape of the filament is crucial, which is given here by the good circularity of the filament cross-section. Furthermore, the powder is apparently homogeneously distributed in the binder, as can be seen from the bright spots (NATP particles) in the SEM images in Figure 2(c–e). This is important to avoid anisotropies in the green part, which would be revealed during post-processing. Due to the high degree of filling, no die swelling that usually occurs with extruded polymers could be seen in the extrudate, since the diameter was slightly smaller than the nozzle opening.^[24,29]

Filaments could be drawn with all feedstocks, however, 3D printing with 60 vol% was unreliable due to annular backflow and nozzle clogging that might cause a print failure. This may be related to the fact that the filling level is close to the critical filling level for the present combination of powder and binder system.^[30] Hence, the following work was continued only with 58 vol% filaments.

Conventionally prepared solid electrolyte pellets were made by cold-isostatically pressing powders to serve as a reference to evaluate the performance of 3D printed samples.

Disk-shaped 3D printed samples were produced using a printing nozzle with a diameter of 0.6 mm. The strands extruded and deposited by the 3D printer usually have a shape

that can be described by a rectangular cross-section with rounded sides.^[31] With a wide nozzle diameter and small layer height, the rounding of the edges of the strands is reduced, thus counteracting the voids that form between deposited strands which are typical in 3D printing.^[32] Hence, to obtain a dense, defect-free green body, a layer height of 100 µm was selected. Very dense printed parts, with no typical voids between the printed material strands, can achieve higher densities during subsequent sintering than a part that has typical 3D printing defects in the form of voids. Therefore, contact necks can easily form and particles can grow together in the sintering process, which is essential to achieve very dense parts. A high density of the electrolyte pellet is especially important for all-solid-state batteries as the sodium-ions diffuse through the ceramic material and any porosity can be considered a “non-conductive” phase, which would reduce the overall ionic conductivity of the material.

Due to a slight contraction of the deposited strand after extrusion, which can occur with very high filled feedstocks,^[25] a correction of 10 µm of the Z-coordinate per layer counteracted the shrinkage of the layer height. The Z-correction to 90 µm per layer enabled printing of defect-free green bodies and homogeneous powder distribution, as shown by the cross-section of a 3D printed sample disk SEM images in Figure 2(d and e). To ensure improved fusion of the layers, the printing speed was adjusted to 5 mm s⁻¹. Due to the slow printing speed, the heat of the nozzle can be maintained on the deposited material for a longer period. The heat facilitates the diffusion of the polymer chains into deposited adjacent strands and into freshly deposited strands. This results in improved interfacial healing between the deposited strands.^[29,33] Even in simple geometries, 3D printing shows vital advantages compared to conventional powder pressing, since neither a powder mold nor a press die is required. This also means that different sample geometries or pellet diameters can be freely configured. In addition, printing a specimen takes about 10 minutes with the printing parameters used here, and several specimens can be printed automatically one after the other, which means a considerable acceleration in specimen production. A short video of the printing process is provided in the supplementary information.

A two-step debinding process was used to remove the organic components from the printed parts i.e., in a solvent and then thermally. The advantage of a solvent debinding step before thermal debinding is to create an open porous network in the part. The decomposition products released during thermal debinding in gaseous form can thus escape without cracking or bloating the part.^[34] The loss of mass of 3D printed parts with solvent debinding originates from the solubility of a component of the binder system in the selected solvent. In this case, PEG is the soluble component, having the advantage of being highly soluble in water, and accordingly the samples were debinded in demineralized water. Based on previous work by Weber,^[35] debinding was carried out at room temperature to avoid defect formation due to swelling of the backbone polymer at higher solvent temperatures. Figure 2(f) shows the total mass loss of 3D printed samples after 6-, 24- and 48-hours debinding time in demineralized water. After 24 h, no further

significant change in mass was observed, so that the debinding time for the following processing steps was set to 24 h.

A wide range of sintering temperatures was tested on fully debinded printed specimen and pressed powder compacts to approximate the appropriate sintering temperature. Furthermore, deviations in the sintering behavior between printed and pressed powder parts had to be identified. The relative and apparent densities of 3D printed, debinded, sintered samples, and cold-isostatically pressed (CIP) powder compacts acting as a reference, are shown in Figure 3(a). Figure 3(b) depicts the diffractograms of a reference (ICSD Coll. Code 154071), the pristine powder, the printed-sintered parts, and the pressed-sintered parts. The investigated materials displayed the same phase as the ICSD reference which has the $R\bar{3}c$ space group. Further, no significant differences between printed and pressed samples were found. The magnified reflex at 21.8° on the right side of Figure 3(b) shows an AlPO_4 impurity phase formed in small quantities. As observed in the lithium analog $\text{Li}_{1.3}\text{Al}_{0.3}\text{Ti}_{1.7}(\text{PO}_4)_3$, the proportion of the second phase decreases with increasing sintering temperature.^[36]

An applied pressure of approximately 500 MPa, to produce the green body from the pristine powder, led to a green density of $(67 \pm 2)\%$. Whereas, considering the amount of powder in the feedstock, geometry and weight of the 3D printed green part, only a green density of $(53.72 \pm 1.59)\%$ is realized. The samples sintered at 1100°C showed the highest densities regardless of the fabrication process with $(94.27 \pm 0.37)\%$ for 3D printed samples and $(94.27 \pm 0.07)\%$ for pressed powder compacts. The slightly higher deviation for the 3D printed sample might originate from slight inhomogeneities in different samples used for the measurements. The 3D prints sintered at 1000°C had a lower density than pressed samples by approximately 5% because the green densities of the fabricated samples were different. The higher initial compaction of the pressed powders results in more contact points between the powder particles and thereby in an increased sintering activity.^[37] A decrease in density is observable for both, the 3D

printed and pressed samples, sintered at 1200°C in comparison to samples sintered at 1100°C . This might be due to the increased gas pressure of entrapped gas inside closed porosity which causes an enlargement of the pores. This is further verified by SEM Images of the cross sections (see Figure 4(e) and Figure S2) which show large void formations with diameters of up to more than $100\ \mu\text{m}$. The decrease in density is more pronounced for the pressed reference. Considering the high densities of samples sintered at 1100°C , it is very likely that during the heating phase, up to 1200°C , a sufficient density with closed porosity was already achieved at lower temperatures. Further heating increases the gas pressure of the gas (air) trapped inside pores and thus causes an enlargement of the pores.^[38]

Figure 4 shows the microstructure evolution of 3D printed NATP samples with different sintering temperatures. The microstructure and porosity in the cross-sectional images reflect the results of the density measurements. The 1000°C sintered sample shows homogeneously distributed fine pores in Figure 4(a and b). In addition, the inset in Figure 4(b) shows very fine and uniform grain sizes, which conversely means that no pronounced grain growth has yet taken place. In contrast, the sample sintered at 1100°C exhibits a generally denser microstructure with some residual porosity, as seen in Figure 4(c and d). The circular voids present in Figure 4(d) are secondary phase precipitates (AlPO_4 , see Figure 3(b)) removed by the thermal etching. However, these are still visible in unetched samples (see Figure S3). In Figure 4(d), pronounced grain growth is noticeable. In addition, discontinuous grain growth can be seen due to particularly large and few grains. Few intragranular cracks are visible. The sample sintered at 1200°C has particularly large voids Figure 4(e and f). The light-gray colored large holes can be attributed to chipping during grinding and polishing. A higher magnification of a dense region shown in Figure 4(f) reveals more advanced grain growth, but also an increase in the amount of microcracks in the microstructure compared to samples sintered at 1100°C .

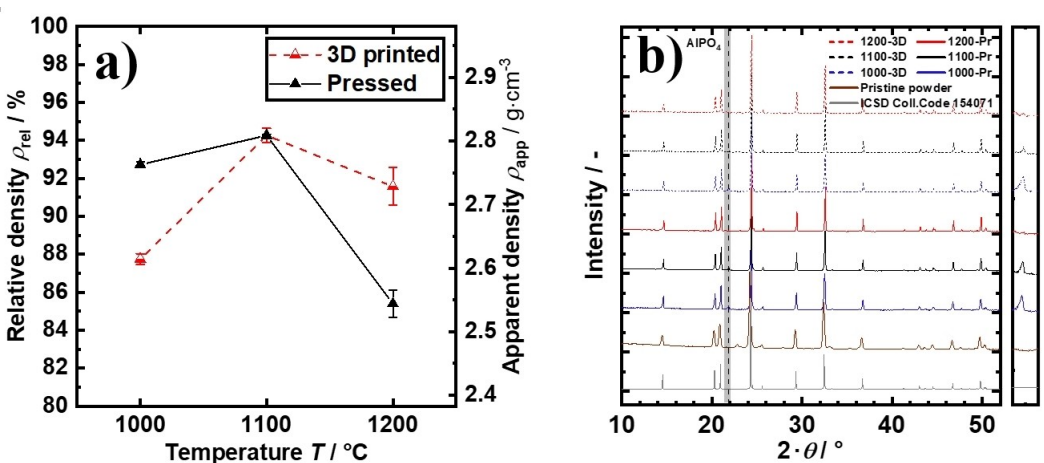


Figure 3. Effect of sintering temperatures on the relative and apparent density of sintered 3D printed and pressed samples at 1000°C , 1100°C and 1200°C in a), and the observed phases in the diffractograms in b) of a reference, the pristine powder, printed and sintered samples, as well as sintered powder compacts.

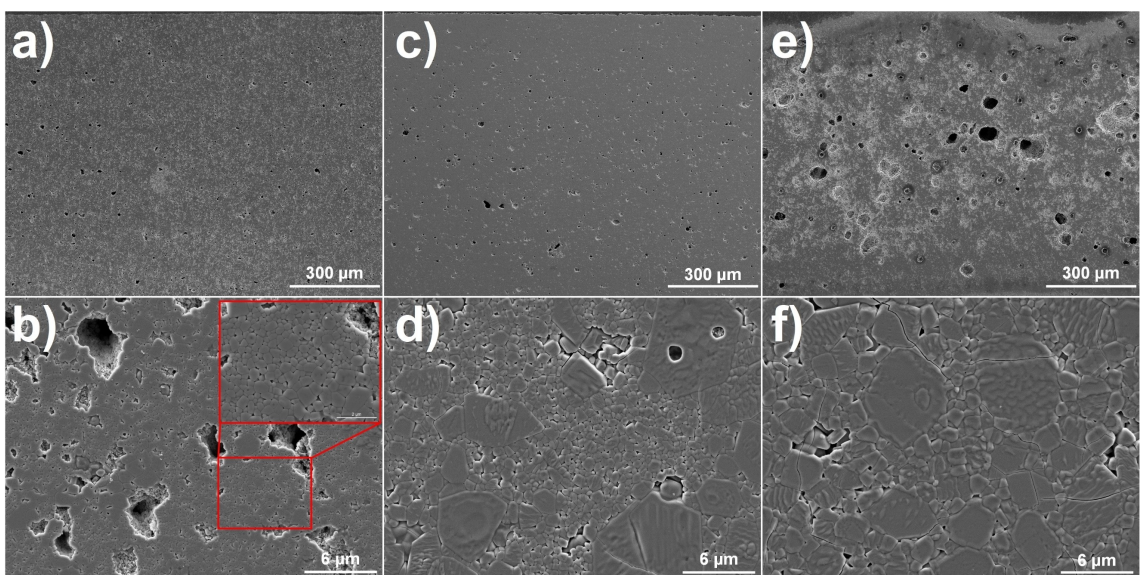


Figure 4. Micrographs of sintered, polished and thermally etched cross sections of 3D printed samples for a) and b) 1000 °C, c) and d) 1100 °C, e) and f) 1200 °C.

A comparison of the microstructures of 3D printed and pressed samples sintered at 1100 °C in Figure 5(a and b) shows a coarse microstructure for the 3D printed sample with respect to the pressed one with approximately the same density of the differently produced specimen (see Figure 3(a)). The particle size distribution of the pristine NATP powder exhibits a bimodal particle size distribution with one fraction at around 140 nm, and a second fraction at slightly below 10 μm particle diameter, as can be seen in Figure S4(a). SEM images in Figure S4(b and c) reveal that most of the larger particle fraction must be agglomerates. Wu and Wei^[39] have shown that processing a feedstock using counter-rotating mixing blades in an internal mixer can lead to the break-up of powder agglomerates. By breaking up the agglomerates, a larger part of the narrow and fine fraction is better distributed in the feedstock (see Figure S5) and thus leads to an increased sintering activity, which promotes an earlier grain growth.^[37,40]

Measured grain size distributions of printed and pressed samples, which were sintered at 1000 °C, 1100 °C and 1200 °C are shown in Figure 5(c). All distributions displayed log-normal distributed grain sizes. It is seen that the pressed and printed samples do not show any significant difference in grain size distribution due to the low sintering temperature of 1000 °C. The most frequent grain size of the 3D printed and 1000 °C sintered (1000-3D) sample is approximately 340 nm, while the most frequent grain size of the pressed reference, sintered at 1000 °C, (1000-Pr) is only slightly higher with 400 nm due to the better densification.

A narrow particle size distribution for 3D printed parts from breaking up the agglomerates in the internal mixer leads to a sufficient density at 1100 °C, where grain growth starts to occur, as seen by the most frequent grain sizes of 0.67 μm for 1100-Pr and almost a doubling with 1.1 μm for 1100-3D.^[37] As expected, the largest most frequent grain sizes of approximately 1.6 μm

for 1200-Pr and 1.8 μm for 1200-3D were measured at the highest sintering temperature of 1200 °C. Due to the increased sintering temperature and the resulting accelerated grain boundary diffusion, abnormal grain growth starts, which is noticeable from the more frequent, significantly larger grains.^[41] These results are also reflected in the median grain sizes, seen in Figure 5(d). While the grain sizes from the 1000 °C and 1200 °C sintered samples (printed and pressed) are very close to each other, a significant increase in the grain size of the 1100-3D compared to the 1100-Pr is evident. The magnitude of the error bar also shows the increasingly abnormal grain growth with sintering temperature. The coarser microstructure of the 1100-3D sample does not seem to decrease the macroscopic mechanical properties of the samples, as the hardness (HV10) value for the 1100-3D material is 446 ± 19, while the hardness of 1100-Pr is 422 ± 22. The slightly higher hardness might be a result of a lower phase content of the secondary phase AlPO₄ in the 1100-3D samples, which is evident by the smaller reflex in the diffractogram shown in Figure 3(b). However, measurements using a nanoindenter show an opposite tendency for the Vickers hardness. While the 1100-3D specimen yields a Vickers hardness (5mN load) of 578.6 ± 82.3, 1100-Pr specimens yield higher values of 777.2 ± 40.9. On one hand, it is quite plausible that this is due to the coarser microstructure of the printed/sintered samples. On the other hand, the higher scatter and number of outliers to lower hardness values for the printed sample (see Figure S6) indicates that there are finer distributed pores, which are either directly affected by the indentation or are pores beneath the indented grains. Furthermore, micro-cracks visible in Figure 4(d) in the SEM image are negatively affecting the hardness of the material. Because the indentation made by the nanoindenter is much smaller due to a significantly lower load (5 mN) than the usually used HV10 (100 N), the measurement indentation tends to reflect the

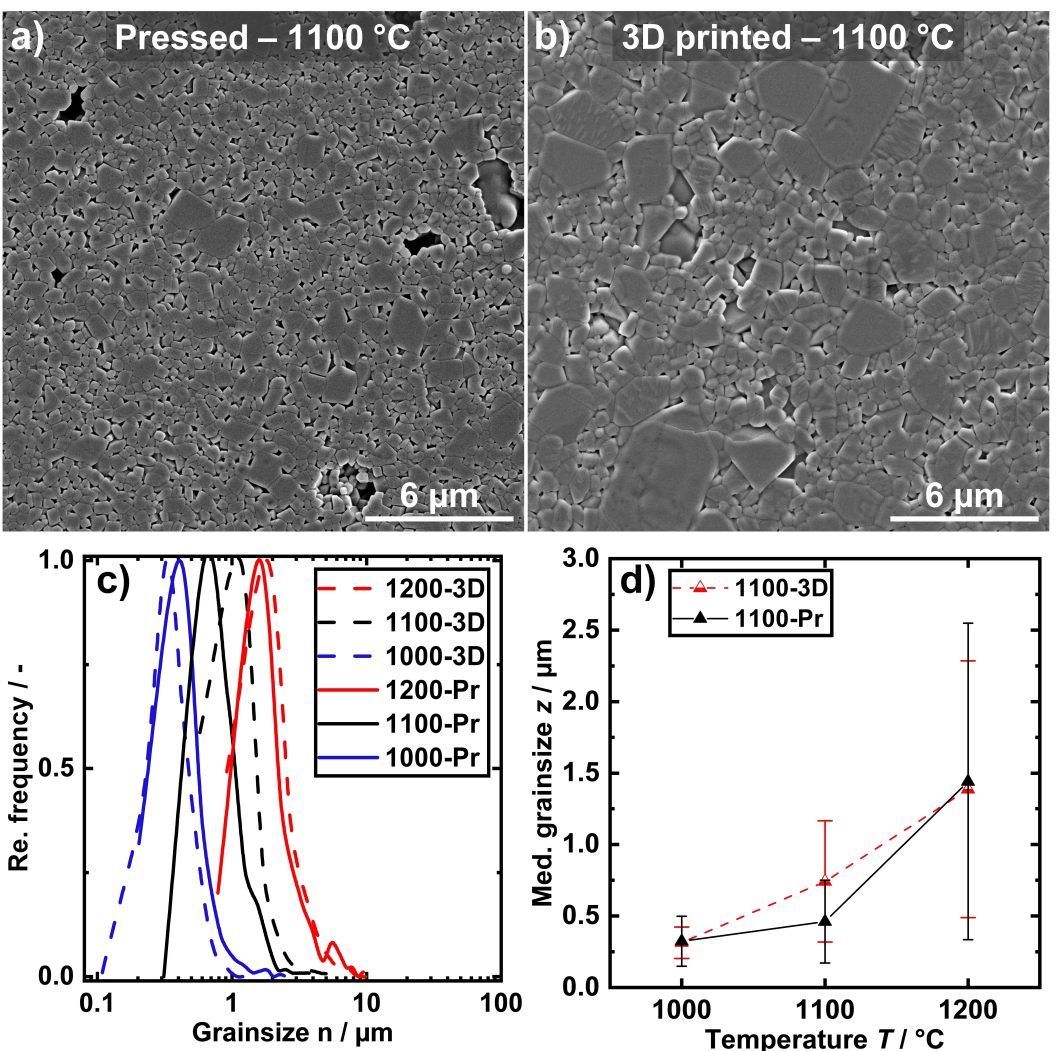


Figure 5. Microstructure comparison of printed and pressed sintered samples. a) Microstructure of the pressed reference and in b) the printed part, both sintered at 1100 °C / 5 h, c) grainsize distribution of sintered 3d printed (dotted lines) and pressed (solid lines) samples at 1000 °C (blue), 1100 °C (black) and 1200 °C (red) for 5 h, d) median grain size of 3D printed (red) and pressed parts (black) sintered at 1000 °C, 1100 °C and 1200 °C. The connecting lines are a guide for the eyes.

physical properties of the material rather than the sample itself. This would also explain the significant fluctuation of the values when a second phase or pore is encountered, as has been reported in literature for other NaSICON materials.^[42] Furthermore, the Young's moduli are determined by the means of a nanoindenter, which are 117.7 ± 8.8 GPa for 1100-3D and 122.9 ± 5.3 GPa for 1100-Pr and these agree well with the values reported for LATP.^[43]

Electrochemical investigations

Figure 6(a) shows the Nyquist plot of the electrochemical impedance spectra of 3D printed and pressed samples that were sintered at 1100 °C / 5 h, measured at 20 °C in the blocking electrodes setup (sputter deposited gold electrodes). The semi-circles for grain and grain boundary, which are typical for oxide electrolytes, can be perceived.^[44] Processes occurring at the

grain and the grain boundary are typically fitted with a parallel circuit of resistor and constant phase element (CPE) in an equivalent circuit, respectively, as shown by the inset in Figure 6(a).^[45] The 3D printed sample shows approximately half the total resistance ($R_{\text{total}} = R_{\text{grain}} + R_{\text{grain boundary}}$) compared to the pressed sample. This signifies the better diffusion of sodium-ions in the 3D printed sample. The ionic conductivity σ_{ionic} can be calculated according to Equation (1).

$$\sigma_{\text{ionic}} = \frac{h}{A \cdot R_{\text{total}}} \quad (1)$$

with h for the pellet thickness, A the area of the electrodes and the total resistance R_{total} . The higher conductivity of the 3D printed samples is a trend evident over the entire measured temperature range of -40 °C to 200 °C, as can be seen in the Arrhenius plot in Figure 6(b). The activation energies are $0.58(45)$ eV and $0.57(52)$ eV for the printed and pressed

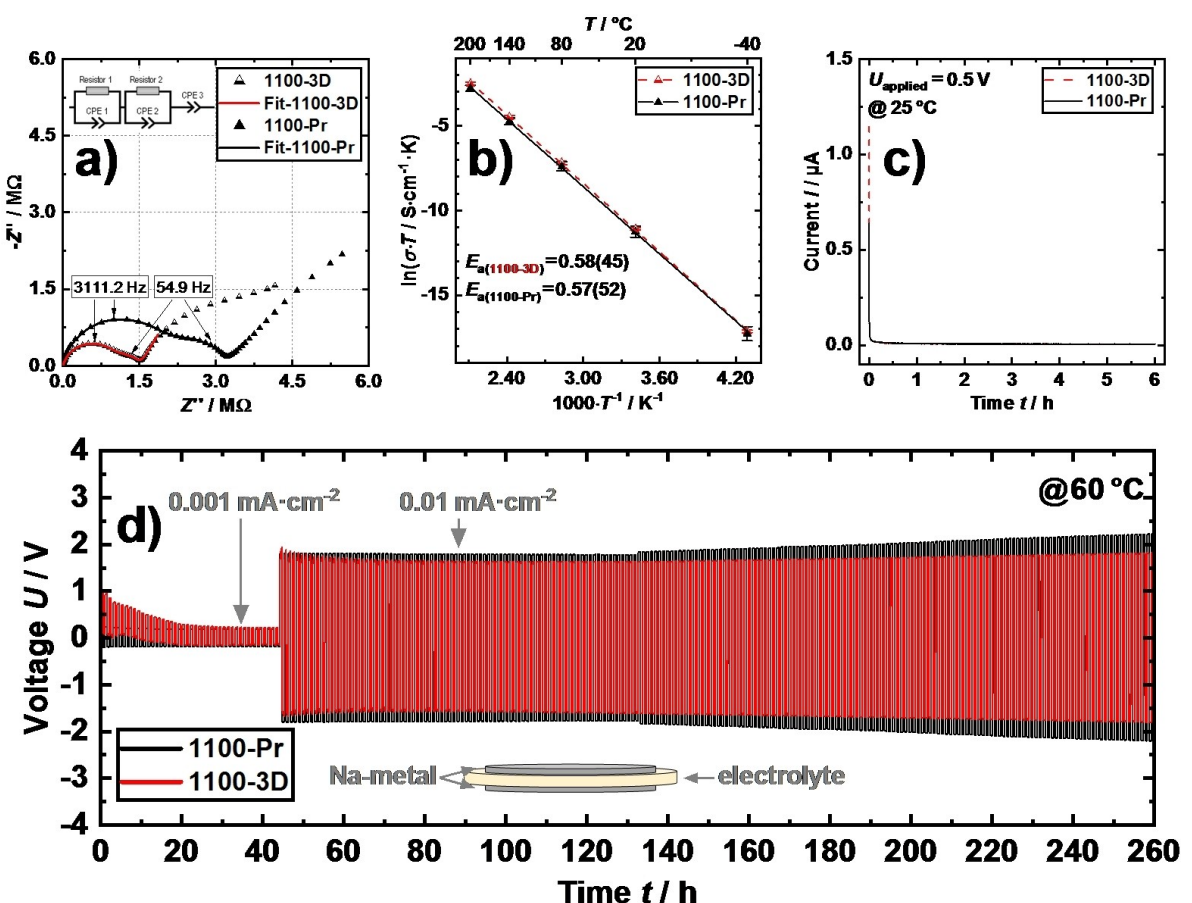


Figure 6. Electrochemical performance of printed and pressed sintered samples. a) exemplary impedance spectroscopy measurements at 20°C and fit in Nyquist representation of a 3D printed (thickness 480 µm) and pressed powder compact (thickness 500 µm), debinded and sintered at 1100 °C for 5 h, b) Arrhenius plot of the ionic conductivities of 1100 °C / 5 h sintered samples (3D printed and pressed powder) with their respective activation energies, c) DC polarization drop measurement of the printed and pressed samples measured at 25 °C with an applied voltage of 0.5 V, d) stripping/plating of printed and pressed samples.

samples, respectively, and are within the range of reported literature values (0.54–0.61) eV.^[46,47] The activation energies are accessible since the ionic conductivity follows the Arrhenius law, with equation (2).

$$\sigma_{\text{ionic}} \cdot T = \sigma_0 \cdot e^{-\left(\frac{E_a}{kT}\right)} \quad (2)$$

where T is the applied temperature, σ_0 the pre-exponential factor, E_a the activation energy and k the Boltzmann constant. The ionic conductivities of samples 1100-3D and 1100-Pr measured at 20 °C are $(0.524 \pm 0.037) \times 10^{-7} \text{ S cm}^{-1}$ and $(0.471 \pm 0.148) \times 10^{-7} \text{ S cm}^{-1}$, respectively, and are also within the range of published data from the literature.^[46,47] The density of the fabricated samples has a major impact on the conductive properties of the material.^[48,36] However, this reasoning can be excluded due to the basically same density of 1100-3D and 1100-Pr samples (see Figure 3(a)). The enhanced ionic conductivity of the 1100-3D samples is mainly attributed to its microstructure. The general larger grain size (see Figure 5) of the 1100-3D sample conversely implies less grain boundaries, which impede ion diffusion, and thereby has a beneficial

influence on the overall ionic conductivity of the printed samples.^[41,49a,b]

The electronic conductivity was estimated by DC polarization as the formation of a carbon coating for feedstocks, containing electrode material, after sintering has been observed in the literature.^[19,20] This would lead to self-discharge or a short-circuit of the cell in the case of a SE. Initially, after applying a voltage, electrons and ions contribute to the measured current, which rapidly decreases after a short time and ends in a plateau where eventually only electrons contribute to the measured current, as can be seen in Figure 6(c).^[50]

From the plateaus of the DC polarization measurement, an electronic conductivity σ_{el} of about $1 \times 10^{-9} \text{ S cm}^{-1}$ for 1100-3D and $2 \times 10^{-9} \text{ S cm}^{-1}$ for 1100-Pr can be determined with Equation (3).

$$\sigma_{\text{el}} = \frac{h \cdot I}{A \cdot U} \quad (3)$$

With the current I and the voltage U . Since no improvement of the electronic conductivity can be observed for the 3D

printed material, an influence on the conductive properties of NATP due to the presence of potential residual carbon after the sintering process can be excluded. The transference number for Na^+ -ions can be determined through DC polarization as well and is close to 1 (> 0.99) for both materials, as has been observed for other NaSICON materials.^[51]

The stripping/plating behavior of the differently manufactured electrolytes was tested using chronopotentiometry at 60 °C in a symmetric setup of Na/1100-3D/Na and Na/1100-Pr/Na cells, respectively, as shown in Figure 6(d). At the lower current density of 1 $\mu\text{A cm}^{-2}$, an initial polarization of 0.5 V is seen for the printed sample, which decreases to about 0.35 V with cycling, which is likely attributed to an improved contact between sodium and the solid electrolyte. On increasing the applied current by one order of magnitude (10 $\mu\text{A cm}^{-2}$), the polarization for the 3D printed sample is slightly lower compared to the pressed sample and remains relatively stable over the following 200 cycles with a polarization of about ± 1.8 V at the end of the measurement. The pressed electrolyte, on the other hand, shows an increase in polarization with cycling of about ± 2.2 V at the end of the measurement. However, the high polarization at the currents used is not sufficient for commercial use due to the low ionic conductivity of NATP. Typically, samples up to 2 mm thick are used for oxide based SE's characterization and the samples for the stripping/plating tests had a thickness of about 700 μm .^[52] By further reducing the thickness, the polarization can be reduced. Another possibility is to use materials with higher ionic conductivity. Nevertheless, the lower polarization and thus lower resistance of 1100-3D is in good agreement with the previous impedance measurements in Figure 6(a and b), which showed better ionic conductivity for the printed sample. Hence, this is a successful study of NASICON based sodium containing solid electrolyte being FFF 3D printed for the first time and evaluated for Na/SE/Na stripping/plating and ionic conductivity. The 3D printed electrolyte demonstrates better stability compared to the pressed SE. Further, in the case of a structured battery, it is also possible to deposit a single layer of electrolyte material between the active materials. This can significantly minimize the resistance in a cell due to the reduced thickness of the electrolyte, which is the objective of future work. Thus, this work proved that with the right process control typical printing artifacts can be avoided and comparable properties to common manufacturing methods of SE can be achieved. This paves the way to use FFF for structured solid-state batteries in order to produce prototypes and to investigate structure-performance correlations in more detail.

Conclusions and Outlook

A full ceramic electrolyte for the application in ASSIB was prepared by 3D printing using the FFF technique for the first time, followed by a two-step debinding and subsequent sintering of the printed samples. Feedstocks with 58 vol% NATP exhibited the best printability and print results at the highest possible amount of ceramic loading. Optimization of the

printing temperature and speed produced the best results at 180 °C and 5 mm s^{-1} . A correction of the layer height from 100 μm to 90 μm in the gcode improved the adhesion between layers, yielding bulk-like specimens. The integrity of the printed parts is ensured after thermal debinding by applying a prior solvent debinding step of 24 hours. The highest relative density for 3D printed and for pressed samples at 1100 °C/5 h was ~94.3%. The feedstock processing for the FFF breaks up agglomerates, which has led to a change in the sintering behavior of the printed samples here and thus also to a coarser microstructure.

Slightly higher ionic conductivities were determined for the printed samples which is likely due to the generally larger grains compared to those of the pressed samples. Carbon coating of the electrolyte particles in the 3D-printed samples after the thermal treatments can be excluded due to negligible electronic conductivity values of both printed and pressed pellets. Stripping/plating tests prove that 3D printed solid electrolytes via FFF are not negatively affected in their function as ion conductors due to possible process-related artifacts, which were prevented in the present work, and thus are in fact a viable option to fabricate solid electrolytes. Therefore, the electrolytes produced in this way can be used in all-solid-state sodium-ion batteries.

Future work will focus on the production of half cells and full cells using a recently commercially available NaSICON material ($\text{Na}_3\text{Zr}_2\text{Si}_2\text{PO}_{12}$) with significantly better ionic conductivity, which will be manufactured using multi-material FFF 3D printing. This enables a printing procedure of a complete full cell in a single step (cathode, solid electrolyte, and anode) and subsequent sintering might result in a reduced interfacial resistance of the electrode and electrolyte and an easier assembly of ASSIB for commercial applications.

Experimental Section

Materials and feedstock preparation

A commercially available solid electrolyte $\text{Na}_{1.3}\text{Al}_{0.3}\text{Ti}_{1.7}(\text{PO}_4)_3$ (NATP, NEI Corp., USA) powder with the typical NASICON (Na Super Ionic CONductor) structure was used without any further modification. The specific surface area measured by utilizing BET (Gemini VII 2390, Micromeritics Corp.) was 2.8 m^2g^{-1} . The He-Pycnometry (Pycnomatic ATC, Porotec) powder density was 2.88 g cm^{-3} . Feedstocks containing the NATP powder, polyvinyl butyral (PVB, Mowital B30H, Kuraray GmbH, Germany), polyethylene glycol (PEG, 4000 g mol⁻¹, Carl Roth GmbH, Germany) and lauric acid (LA, Carl Roth GmbH, Germany) were kneaded in a torque recording measuring mixer (W50 EHT, Brabender GmbH) at 125 °C for 1 h at a constant rotation speed of the counter rotating mixing blades of 30 rpm according to the quantities given in Table 1. Approximately a quarter to a third of the NATP powder is filled together with the lauric acid into the chamber, accompanied by the addition of PVB and PEG. The rest of the NATP powder is added after the PVB and PEG are softened. The amount of surfactant was based on the specific surface area of the NATP with 3.3 mg lauric acid per m^2 NATP in the feedstock. The binder system composition is a 1:1 volume ratio of PVB and PEG + LA. All feedstock components were dried under vacuum at 47 °C overnight before use.

Table 1. Feedstock compositions for three different solid loadings.

Electrolyte	[vol %]	Backbone	[vol %]	Plasticizer	[vol %]	Surfactant	[vol %]
NATP	55	PVB	22.5	PEG	21.0	Lauric acid	1.5
	58		21.0		19.4		1.6
	60		20.0		18.3		1.7

Viscosity

Shear-rate-depending viscosity was measured using a capillary rheometer (Rheograph 25, Göttfert) at 160 °C with a capillary opening of 1 mm, 30 mm length and 180° inlet angle. 160 °C is assumed to be the potential printing temperature and therefore served as a starting point for 3D printing. The Weissenberg-Rabinowich model was applied to correct the measured data.

Filament winding

Feedstocks containing 55, 58 and 60 vol% NATP in granular form were extruded into filaments using a single screw extruder (Noztek pro HT, Noztek) with a nozzle diameter of 2.8 mm at 100 °C and wound onto a commercial filament spool using an automated winder (The Winder 1.0, Noztek) as depicted in Figure 2(c) for 58 vol% feedstock.

3D printing

58 vol% feedstock was used for 3D printing and the filament spool was placed on top of the 3D printer (modified German RepRap 350 pro). Disk-shaped 3D models were created in a CAD software (Autodesk fusion 360) with a diameter of 12 mm and a height of 1.5 mm. The model was then loaded into a slicer software (Cura) where the printing parameters were set. A correction of the layer height was performed in the generated gcode from 100 µm to 90 µm to achieve a better interface healing/welding between the deposited and depositing material strands. The infill density was set to 105% to overfill the infill of the part and thereby close gaps between the deposited material strands. The printing pattern was chosen as lines and the printing direction turned by 90° per layer. Printing temperature was 180 °C without part cooling. The bed temperature was set to 60 °C for a better bed adhesion and it was printed on an adhesive tape (TESA). Printing speeds of up to 25 mm s⁻¹ were possible but yielded low quality parts. Best print quality was achieved with a printing speed of 5 mm s⁻¹.

Thermal treatment

The printed parts were solvent debinded in demineralized water at room temperature for 6 h, 24 h and 48 h, respectively. After drying for several hours, the parts were weighted and then placed on a powder bed in a crucible and thermally debinded up to 500 °C in a furnace (HT6/28, Carbolite) with intermediate holding steps of one hour at (150, 250, 330, 400 and 500) °C and a slow heating rate of 0.5 K min⁻¹ under normal atmosphere.

The completely debinded specimens were sintered in a muffle oven (RHF 17/3, Carbolite) at three different temperatures of 1000 °C, 1100 °C and 1200 °C for 5 h in air with a heating and cooling rate of 5 K min⁻¹. Reference specimens were prepared by cold isostatic pressing (KIP 300 E, Paul-Otto Weber GmbH) of NATP powder at about 500 MPa and sintered the same way as the printed specimen.

XRD

Diffractograms of the pristine powder and sintered, polished pellets were measured with a monochromator equipped Empyrean X-ray diffractometer (Malvern Panalytical) using Cu_{Kα} radiation in a 2θ range of 10°–52° with a step size of 0.013°.

Density

Density measurements were performed three times per printed or pressed pellet and three pellets per sample type according to Archimedes principle (SECURA225D-1s, Sartorius Lab Instruments GmbH & Co. KG) with water as liquid medium. The green density was geometrically determined with 15 samples for 3D printed specimen and 7 samples for the pressed pellets.

Microstructure analysis

The microstructural investigations of sintered pellets cross-sections were performed via SEM (XL 30 S, Philips). The sintered pellets were grinded subsequently with sandpapers of 800, 1000, 2500 and 4000 grits, followed by subsequent polishing with diamond suspensions of 3 µm, 1 µm and 0.25 µm. The polished surfaces were then thermally etched at 800 °C in air for 10 min with a heating and cooling rate of 10 K min⁻¹. A thin gold layer was sputtered on the specimen for SEM images, taken at an accelerating voltage of 5 kV. At least 500 grains were measured per material for the grain size distribution with the open-source software ImageJ.

Hardness

Indentation was performed with a Vicker pyramid setup (Reicherter c. Stiefelmayer KG) with an applied load *F* of 98.06 N and a holding time of 5 seconds. The length of the diagonals *d* of the indents were measured in a SEM and the hardness was calculated according to Equation (4). Five indents were averaged for pressed/sintered (1100 °C) and 3D printed/sintered (1100 °C) pellets, respectively.

$$HV10 = 0.1891 \times \frac{F}{d^2} \quad (4)$$

Nanoindentation was performed with 5 mN load and 10 s holding time (Nanohärtetest: NHT3, Anton Paar). 23 indents for 3D printed/sintered and 25 indents for pressed/sintered samples were evaluated for the hardness and Young's modulus.

Electrochemical impedance measurement

The sintered pellets were grinded in the same way as the samples for microstructure investigation up to 4000 grit sandpaper and then sputtered with gold on both sides (25 mA, 120 s, Sputter Coater, Structure Probe Inc.). The measurement was performed on

an analyzer for electrochemical impedance spectroscopy (NEISYS, Novocontrol Technologies) with a perturbation voltage of 50 mV from -40 to 200°C under flowing nitrogen gas. The measurements were performed in increments of 60°C and for each temperature one hour waiting time was set to acquire thermal equilibrium. Three pellets per sample type were measured.

Chronoamperometry

Electronic conductivity was measured with a Biologic VMP3 in a battery holder (BH-1i, Biologic) on pellets that were prepared in the same way as for the impedance measurements. A DC potential of 0.5 V for 6 h at 25°C was applied and the current vs. time was recorded until a stable steady state region established with which the electronic conductivity can be estimated.

Stripping/plating

The sodium metal was pressed on both sides of sintered-polished (4000 grit) pellets (thickness $\sim 700\text{ }\mu\text{m}$) and pressed with a uniaxial press (1000 psi, MSK-110, MTI Corp.) to establish a good interfacial contact between Na-metal and electrolyte. The pellet was then placed into a spring-loaded cell (TSC Battery, rhd instruments) and transferred to a climate chamber which was set to 60°C . The system was given 2 hours to establish thermal equilibrium. All cell assembly was done in a glovebox (UNILab pro, MBraun) under argon atmosphere with $<0.1\text{ ppm H}_2\text{O}$ and O_2 . Each stripping/plating cycle was carried out for 1 h , and the first 40 cycles were performed with a current density of $1\text{ }\mu\text{A cm}^{-2}$. The following cycles were measured with an applied current density of $10\text{ }\mu\text{A cm}^{-2}$.

Acknowledgements

This work contributes to the research performed at CELEST (Center for Electrochemical Energy Storage Ulm-Karlsruhe) and was funded by the German Research Foundation (DFG) under Project ID 390874152 (POLiS Cluster of Excellence, EXC 2154). In addition, Ms. Jung is thanked for the SEM images, Ms. Offermann and Ms. Bohn are thanked for the measurements of particle size distribution, BET and He-pycnometry. Mr. Reuters and Mr. Hofmann are thanked for providing test-cells for stripping-plating tests and fruitful discussions. Mr. Ott is thanked for performing the XRD measurements. Mr. Bolich is thanked for performing the Vickers indentation. Ms. Reif is thanked for performing the nanoindentation tests. Open Access funding enabled and organized by Projekt DEAL.

Conflict of Interests

The authors declare no conflict of interest.

Data Availability Statement

The raw data of relevant measurements is available in Zenodo for open access at DOI: <https://doi.org/10.5281/zenodo.10057982>.

Keywords: 3D printing · FFF · solid electrolyte · sodium-ion battery · solid-state

- [1] a) H.-K. Roh, H.-K. Kim, M.-S. Kim, D.-H. Kim, K. Y. Chung, K. C. Roh, K.-B. Kim, *Nano Res.* **2016**, *9*, 1844; b) M.-Y. Wang, J.-Z. Guo, Z.-W. Wang, Z.-Y. Gu, X.-J. Nie, X. Yang, X.-L. Wu, *Small* **2020**, *16*, e1907645.
- [2] D. Wang, Q. Liu, C. Chen, M. Li, X. Meng, X. Bie, Y. Wei, Y. Huang, F. Du, C. Wang et al., *ACS Appl. Mater. Interfaces* **2016**, *8*, 2238.
- [3] D. Larcher, J.-M. Tarascon, *Nat. Chem.* **2015**, *7*, 19.
- [4] Q. Ma, C.-L. Tsai, X.-K. Wei, M. Heggen, F. Tietz, J. T. S. Irvine, *J. Mater. Chem. A* **2019**, *7*, 7766.
- [5] S. Wang, H. Xu, W. Li, A. Dolocan, A. Manthiram, *J. Am. Chem. Soc.* **2018**, *140*, 250.
- [6] Z. Li, P. Liu, K. Zhu, Z. Zhang, Y. Si, Y. Wang, L. Jiao, *Energy Fuels* **2021**, *35*, 9063.
- [7] a) J. Janek, W. G. Zeier, *Nat. Energy* **2016**, *1*; b) Y. Xiao, L. J. Miara, Y. Wang, G. Ceder, *Joule* **2019**, *3*, 1252; c) M. Guin, S. Indris, M. Kaus, H. Ehrenberg, F. Tietz, O. Guillon, *Solid State Ionics* **2017**, *302*, 102.
- [8] a) S. Naqash, Q. Ma, F. Tietz, O. Guillon, *Solid State Ionics* **2017**, *302*, 83; b) S. Narayanan, S. Reid, S. Butler, V. Thangadurai, *Solid State Ionics* **2019**, *331*, 22; c) H. Park, K. Jung, M. Nezafati, C.-S. Kim, B. Kang, *ACS Appl. Mater. Interfaces* **2016**, *8*, 27814; d) Z. Sun, Y. Zhao, Q. Ni, Y. Liu, C. Sun, J. Li, H. Jin, *Small* **2022**, *18*, e2200716.
- [9] L. Wei, S.-T. Liu, M. Balaish, Z. Li, X.-Y. Zhou, J. L. Rupp, X. Guo, *Mater. Today* **2022**, *58*, 297.
- [10] a) J. Wang, Q. Sun, X. Gao, C. Wang, W. Li, F. B. Holness, M. Zheng, R. Li, A. D. Price, X. Sun et al., *ACS Appl. Mater. Interfaces* **2018**, *10*, 39794; b) T.-S. Wei, B. Y. Ahn, J. Grotto, J. A. Lewis, *Adv. Mater.* **2018**, *30*, e1703027.
- [11] Y. Pang, Y. Cao, Y. Chu, M. Liu, K. Snyder, D. MacKenzie, C. Cao, *Adv. Funct. Mater.* **2020**, *30*, 1906244.
- [12] J. Yan, S. Huang, Y. von Lim, T. Xu, D. Kong, X. Li, H. Y. Yang, Y. Wang, *Mater. Today* **2022**, *54*, 110.
- [13] D. W. McOwen, S. Xu, Y. Gong, Y. Wen, G. L. Godbey, J. E. Gritton, T. R. Hamann, J. Dai, G. T. Hitz, L. Hu et al., *Adv. Mater.* **2018**, *30*, e1707132.
- [14] Z. Liu, X. Tian, M. Liu, S. Duan, Y. Ren, H. Ma, K. Tang, J. Shi, S. Hou, H. Jin et al., *Small* **2021**, *17*, e2002866.
- [15] a) J. Liu, T. Liu, Y. Pu, M. Guan, Z. Tang, F. Ding, Z. Xu, Y. Li, *RSC Adv.* **2017**, *7*, 46545; b) R. Murugan, V. Thangadurai, W. Weppner, *Angew. Chem.* **2007**, *46*, 7778; c) I. N. David, T. Thompson, J. Wolfenstine, J. L. Allen, J. Sakamoto, *J. Am. Ceram. Soc.* **2015**, *98*, 1209.
- [16] M. Kotobuki, *Phys. Status Solidi* **2022**, *259*, 2100520.
- [17] C. W. Foster, M. P. Down, Y. Zhang, X. Ji, S. J. Rowley-Neale, G. C. Smith, P. J. Kelly, C. E. Banks, *Sci. Rep.* **2017**, *7*, 42233.
- [18] C. Reyes, R. Somogyi, S. Niu, M. A. Cruz, F. Yang, M. J. Catenacci, C. P. Rhodes, B. J. Wiley, *ACS Appl. Energ. Mater.* **2018**, *1*, 5268.
- [19] J. F. Valera-Jiménez, J. C. Pérez-Flores, M. Castro-García, J. Canales-Vázquez, *Appl. Mater. Today* **2021**, *25*, 101243.
- [20] M. E. Sotomayor, C. d. La Torre-Gamarra, W. Bucheli, J. M. Amarilla, A. Varez, B. Levenfeld, J.-Y. Sanchez, *J. Mater. Chem. A* **2018**, *6*, 5952.
- [21] A. Maurel, M. Haukka, E. MacDonald, L. Kivijärvi, E. Lahtinen, H. Kim, M. Armand, A. Cayla, A. Jamali, S. Grugeon et al., *Addit. Manuf.* **2021**, *37*, 101651.
- [22] A. Maurel, S. Grugeon, B. Fleutot, M. Courty, K. Prashantha, H. Tortajada, M. Armand, S. Panier, L. Dupont, *Sci. Rep.* **2019**, *9*, 18031.
- [23] R. Eickhoff, S. Antusch, S. Baumgärtner, D. Nötzel, T. Hanemann, *Materials* **2022**, *15*, 6442.
- [24] D. Nötzel, R. Eickhoff, T. Hanemann, *Materials* **2018**, *11*, 1463.
- [25] M. M. Rueda, M.-C. Auscher, R. Fulchiron, T. Périé, G. Martin, P. Sonntag, P. Cassagnau, *Prog. Polym. Sci.* **2017**, *66*, 22.
- [26] D. Nötzel, T. Hanemann, R. Eickhoff, *Keram. Z.* **2019**, *71*, 56.
- [27] a) I. Özden, A. Iveković, A. Kocjan, *Open Ceram.* **2021**, *6*, 100129; b) J. W. Oh, W. S. Lee, S. J. Park, *Powder Technol.* **2017**, *311*, 18; c) L. Gorjan, C. Galusca, M. Sami, T. Sebastian, F. Clemens, *Addit. Manuf.* **2020**, *36*, 101391.
- [28] R. Heldele, *Entwicklung und Charakterisierung von Formmassen für das Mikropulverspritzgießen*. Albert-Ludwigs-Universität Freiburg, 2008.
- [29] A. Das, E. L. Gilmer, S. Biria, M. J. Bortner, *ACS Appl. Polym. Mater.* **2021**, *3*, 1218.
- [30] P. Thomas-Vielma, A. Cervera, B. Levenfeld, A. Várez, *J. Eur. Ceram. Soc.* **2008**, *28*, 763.
- [31] S. Bakrani Balani, F. Chabert, V. Nassiet, A. Cantarel, *Addit. Manuf.* **2019**, *25*, 112.

- [32] a) M. Orlovska, Z. Chlup, L. Bača, M. Janek, M. Kitzmantel, *J. Eur. Ceram. Soc.* **2020**, *40*, 4837; b) Y. Tao, F. Kong, Z. Li, J. Zhang, X. Zhao, Q. Yin, D. Xing, P. Li, *J. Mater. Sci. Technol.* **2021**, *15*, 4860; c) W. Lengauer, I. Duretek, M. Fürst, V. Schwarz, J. Gonzalez-Gutierrez, S. Schuschnigg, C. Kukla, M. Kitzmantel, E. Neubauer, C. Lieberwirth et al., *Int. J. Refract. Met. Hard Mater.* **2019**, *82*, 141.
- [33] M. E. Mackay, *J. Rheol.* **2018**, *62*, 1549.
- [34] S. Rolere, U. Soupremanien, M. Bohnke, M. Dalmasso, C. Delafosse, R. Laucournet, *J. Mater. Process. Technol.* **2021**, *295*, 117163.
- [35] O. Weber, *Wasserlösliche Bindersysteme zum minimieren von Pulver-Binder-Segregationseffekten im Mikropulverspritzguss*. Albert-Ludwigs-Universität Freiburg, **2015**.
- [36] B. Davaasuren, F. Tietz, *Solid State Ionics* **2019**, *338*, 144.
- [37] J. Ma, L. C. Lim, *J. Eur. Ceram. Soc.* **2002**, *22*, 2197.
- [38] R. Telle (Hrsg.) *Keramik*, Springer, Berlin, Heidelberg, **2007**.
- [39] R.-Y. Wu, W.-C. J. Wei, *J. Am. Ceram. Soc.* **2005**, *88*, 1734.
- [40] K. G. Ewsuk, D. T. Ellerby, C. B. DiAntonio, *J. Am. Ceram. Soc.* **2006**, *89*, 2003.
- [41] S. Naqash, D. Sebold, F. Tietz, O. Guillon, *J. Am. Ceram. Soc.* **2019**, *102*, 1057.
- [42] J. M. Valle, C. Huang, D. Tatke, J. Wolfenstine, W. Go, Y. Kim, J. Sakamoto, *Solid State Ionics* **2021**, *369*, 115712.
- [43] J. Wolfenstine, J. L. Allen, J. Sakamoto, D. J. Siegel, H. Choe, *Ionics* **2018**, *24*, 1271.
- [44] J. T. S. Irvine, D. C. Sinclair, A. R. West, *Adv. Mater.* **1990**, *2*, 132.
- [45] T. Polczyk, W. Zajac, M. Ziabka, K. Świerczek, *J. Mater. Sci.* **2021**, *56*, 2435.
- [46] F. E. Mouahid, M. Bettach, M. Zahir, P. Maldonado-Manso, S. Bruque, E. R. Losilla, M. A. G. Aranda, *J. Mater. Chem.* **2000**, *10*, 2748.
- [47] M. Rohde, I. U. I. Mohsin, C. Ziebert, H. J. Seifert, *Int. J. Thermophys.* **2021**, *42*.
- [48] E. C. Bucharsky, K. G. Schell, T. Hupfer, M. J. Hoffmann, M. Rohde, H. J. Seifert, *Ionics* **2016**, *22*, 1043.
- [49] a) K. Okubo, H. Wang, K. Hayashi, M. Inada, N. Enomoto, G. Hasegawa, T. Osawa, H. Takamura, *Electrochim. Acta* **2018**, *278*, 176; b) M. J. Wang, J. B. Wolfenstine, J. Sakamoto, *Adv. Funct. Mater.* **2020**, *30*, 1909140.
- [50] E. M. Hitz, H. Xie, Y. Lin, J. W. Connell, G. W. Rubloff, C.-F. Lin, L. Hu, *Small Structures* **2021**, *2*, 2100014.
- [51] V. Ramar, S. Kumar, S. R. Sivakkumar, P. Balaya, *Electrochim. Acta* **2018**, *271*, 120.
- [52] Q. Ma, T. Ortmann, A. Yang, D. Sebold, S. Burkhardt, M. Rohnke, F. Tietz, D. Fattakhova-Rohlfing, J. Janek, O. Guillon, *Adv. Energy Mater.* **2022**, *12*.

Manuscript received: September 15, 2023

Revised manuscript received: October 31, 2023

Accepted manuscript online: November 3, 2023

Version of record online: November 20, 2023